

Molecular dynamics simulation based size and rate dependent constitutive model of polystyrene thin films

Fan Yang · Somnath Ghosh · L. James Lee

Received: 23 March 2012 / Accepted: 15 April 2012 / Published online: 1 May 2012
© Springer-Verlag 2012

Abstract Rate and size-dependent properties dominate the mechanical behavior of polymeric thin films used in a variety of applications related to generation, transmission and storage of energy. In this paper, molecular dynamics (MD) simulations of polystyrene thin films are used to develop a size and rate dependent finite deformation elastic–plastic constitutive relations. Different modes of deformation are considered in the MD model, and results of simulations are homogenized to yield parametric representations of the constitutive model. The hyperelastic behavior is represented by a modified Ogden type model for films of different thicknesses at different strain rates. The MD simulations suggesting a rate-dependent yield strength is developed for a perfect plasticity model with mitigated size effects. The softer material properties of thin films are found to be the consequence of a large surface layer, which has a low density with high local chain mobility.

Keywords Constitutive law · Polystyrene thin films · Molecular dynamics · Size dependent · Rate dependent

For the special issue in honor of the 25th anniversary of the journal Computational Mechanics entitled Materials for modern energy applications.

F. Yang
Center for Affordable Nanoengineering of Polymeric Biomedical Devices, The Ohio State University, Columbus, OH 43210, USA

S. Ghosh (✉)
Departments of Civil and Mechanical Engineering,
Johns Hopkins University, Baltimore, MD 21218, USA
e-mail: sghosh20@jhu.edu

L. J. Lee
Department of Chemical and Biomolecular Engineering,
The Ohio State University, Columbus, OH 43210, USA

1 Introduction

Polymers are increasingly being used in numerous renewable energy applications for generation, transmission and storage of energy. Such applications include photovoltaic module components, battery and fuel cell membranes, insulation for electrical wires and cables, wind turbine blades etc. Even at the nanoscale, emerging polymeric devices have shown tremendous potential in various applications. This has led to wide-spread research for understanding mechanisms that govern their properties at the nanoscale [1]. Amongst polymers, polystyrene (PS) thin films are widely studied, primarily for their abundant applications and available experimental data. For example, the use of extruded PS fiberglass and foam in domestic and commercial insulation has been proven to have enormous benefits in energy conservation. Polystyrene sheets of 10–100 nm thickness are also used for coating, in the encapsulation of nano-powders to enhance the chemical stability of ultra-fine energetic materials. It is important to understand the properties of PS thin films at the nanoscale. Various anomalous properties have been observed for the thin films with thickness below 100 nanometers, such as lower density, larger free volume and reduced glass transition temperature T_g [2–5]. These size dependent anomalous properties are believed to come from the effect of configurational constraints at the surface and interface [2,3,6–8]. With respect to mechanical properties, several experiments [9,10] and simulations [11,12] have shown that properties of thin films deviate from bulk as the thickness decreases below 30 or 40 nm. Rate dependence is a well known mechanical property for polymer materials and is believed to be also important for PS thin films [3,12]. However, there is a paucity of appropriate size and rate dependent constitutive laws that govern the behavior of thin films, especially with respect to variation along the thickness direction.

Among various experimental techniques, nanoindentation is widely used to measure mechanical properties of micro- and nano-structures [9, 13–15]. However, this technique is not able to accurately determine size dependence for thin films due to strong far field effects from the substrate and the indenter [9, 16]. Recently, a nanoparticle embedding method [17–19] has been developed to investigate the surface layer properties of polymer thin films. In this method, gold particles are placed on polymer thin films and the specimens are annealed at pre-specified temperatures. The embedding depths are tracked during the process using atomic force microscopy (AFM). The final embedding depth is found to be larger on thinner films at temperatures below T_g [19]. In the explanation of these experiment results, there is considerable disagreement on whether a liquid like layer exists near the surface [20, 21]. Another technique is to utilize wrinkling instability of thin films, bonded to a compliant substrate, and deduce the film modulus from the wrinkle wavelength [10, 22]. Deviation of the modulus from bulk was reported for thin films with thicknesses below 40 nm. Since these experiments can only be carried out on the substrate-supporting specimens, the surface effect and the substrate effect cannot be determined separately [7, 9]. Thus obtaining material constitutive laws for very thin polymer films from experiments data is a considerable challenge.

Computer simulation based studies, on the other hand, can be useful in understanding the mechanical property of polymeric thin films. However, finite element method (FEM) suffers from a lack of appropriate size-dependent continuum constitutive laws for modeling polymeric nanostructures. Inverse methods like genetic algorithms or gradient-based optimization [23] that use macroscopic experimental data to get continuum constitutive parameters often result in non-robust constitutive laws. Therefore, methods of bottom-up homogenization [24] using simulations at lower scales, such as molecular dynamics (MD) simulations are desirable in this respect. However, direct MD simulations of thin films undergoing the nanoindentation or nanoparticle embedding process face considerable difficulty due to the small time and spatial scales. The radius of the indenter tip in nanoindentation and the embedded particles in embedding experiments are of the order of 10 nm, while the thickness of the PS thin films is in the tens of nanometers. Correspondingly, the MD simulation box needs to cover at least one million united atoms in the explicit polymer chain structure to capture the experimental domains of these thin films. Accounting for the long relaxation times of PS molecules exceeds the feasible computational scales and capability of currently available computer resources. A more feasible approach is to use bottom-up homogenization, based on MD simulations of representative molecular domains undergoing simple deformation processes, to develop size-dependent constitutive laws. The size-dependent and rate-dependent constitutive models

may subsequently be used to carry out continuum FE analysis of the nanostructures and thin films.

There is a considerable body of literature that has used MD simulations to investigate the mechanical properties of polymers for both bulk and nanostructures. Some of these works have investigated the elastic behavior, yielding and hardening of bulk PS under different pressure, thermal history, and deformation modes using a coarse grained model [25–27]. Simoes et al. [28] have investigated the viscoelastic properties of glassy polymers using a bead spring model. van Workum and de Pablo [29] have calculated the modulus of nano-scale cantilever plates by exerting deflection or compression deformation to the cantilever and using the strain fluctuations method. All of these approaches have shown lower Young's modulus as the structure size decreases. Yoshimoto et al. [12] have simulated the oscillations of free-standing polymer films to investigate the local dynamic mechanical properties using a bead spring model. Their calculations indicate a melt-like region near the free surface by comparing the storage modulus and the loss modulus. Although these efforts have provided valuable insight into the deformation mechanisms at the atomic level and revealed size-dependence of mechanical properties, satisfactory constitutive laws are not well established. Thus quantitative construction of size-dependent constitutive laws is an important task for continuum modeling of nanostructures.

The present work is aimed at the development of a size and rate dependent constitutive law of PS or PS thin films from MD simulations of deformation. Details on the MD simulation model are given in Sect. 2. A constitutive law is proposed in Sect. 3, for which, parameters are calibrated from simulation data of molecular systems with different sizes, configurations and loading conditions to investigate the size and rate dependence. Discussions on the size-dependence are given in Sect. 4.

2 Molecular dynamics model of the polystyrene system

2.1 Inter-atomic potentials

The MD model developed for PS in this analysis is based on prior work by Ghosh et al. [30–32]. The MD simulations are conducted with the general-purpose molecular simulation package LAMMPS [33] that employs an efficient domain decomposition parallelization strategy. The simulations use the leapfrog Verlet and velocity Verlet time integration algorithms for integrating the Newton's equations for motion of the system subject to molecular mechanics force fields. The molecular force field for PS consists of intra-molecular or bonded, and intermolecular or non-bonded interactions. A united-atom representation, discussed in [31, 32], is applied to the PS chain model. The Transferable Potentials for Phase

Equilibria (TraPPE) potential functions [34,35] are used to model the interactions between the united atoms, specifically using a harmonic bond potential as proposed in Han and Boyd [36]. The corresponding total potential energy is expressed as:

$$\begin{aligned}
 U = & \frac{1}{2}k_B(r - r_0)^2 + \frac{1}{2}k_\theta(\theta - \theta_0)^2 \\
 & + \frac{1}{2} \sum_{j=1}^3 k_\phi^j \cos \left[1 + (-1)^{j+1} j \phi \right] \\
 & + \frac{1}{2}k_\psi(\psi - \psi_0)^2 + 4\epsilon \left[\left(\frac{\sigma}{r}\right)^{12} - \left(\frac{\sigma}{r}\right)^6 \right] \quad (1)
 \end{aligned}$$

Terms on the right hand side correspond to stretch, angle, dihedral and improper bonded energy, and the Lennard–Jones (LJ) non-bonded energy functions, respectively. Values of the parameters have been given in [31,32]. A cut-off radius r_{co} of 12 Å [31] is used for the non-bonded interactions.

2.2 Generating computational specimens

A series of free-standing film computational models of PS with varying thicknesses are generated as shown in Fig. 1. For thin film representation, periodic boundary conditions are imposed in the horizontal direction, while finite boundary conditions are imposed in the vertical direction. All molecules in these specimens are mono-dispersed atactic PS chains with 200 monomers per chain. This yields a molecular weight of MW=21 k. The initial configuration is generated using the augmented phantom chain growth or PCG

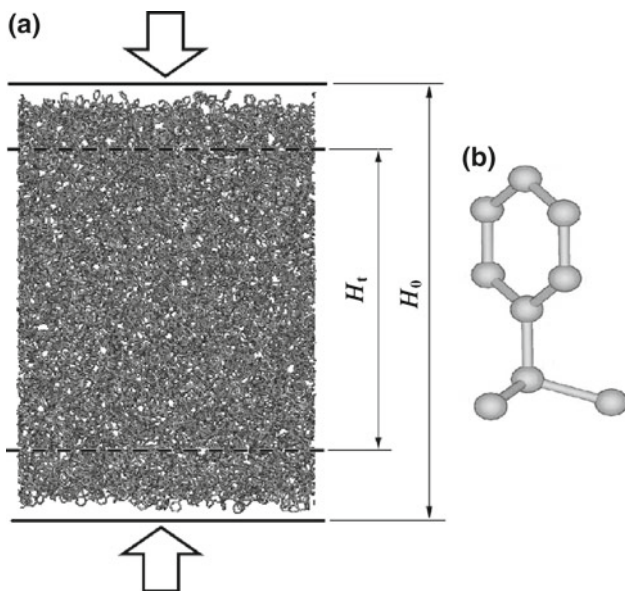


Fig. 1 (a) Initial configuration of simulation system for a PS film of thickness 12.3 nm, and (b) schematic representation of a single monomer in the united-atom model. Bold line and dashed lines indicate the positions of the walls before and after deformation

scheme discussed in [31]. An additional criterion that chains along the non-periodic direction are within a pre-estimated bound is imposed. The chain positions are estimated according to the system size. The initial simulation box has a fixed cross-section of 8 nm × 8 nm, while the height or thickness is varied for different specimens with different number of PS molecules.

After the polymer chain creation, the system is relaxed to push apart physically unrealistic entanglements or overlapped atoms to prevent the system configuration from blowing up. Two methods can be used for this purpose. One is to apply a soft potential as $E(r) = A[1 + \cos(\pi r/r_c)]$ $r < r_c$ instead of the L–J potential for the non-bonded interactions. The other is to perform constant NVE simulation with a limit on the maximum distance an atom can move in each time step. Both methods are tested and found to render configurations of similar densities after further relaxation. The NVE simulation-based latter method is subsequently used for all simulations. The limiting distance ranges from 0.0001 to 0.001 nm and the time step from 0.01 to 1 fs, for a total of 300,000 time steps. For comparing results, a bulk simulation specimen containing 8 PS molecules with 320 monomers per molecule is also prepared. The simulation specimen is generated and dynamically relaxed in a manner similar to the film specimens, except for the fact that all boundaries are periodic. This bulk PS system has been the subject of rigorous validation in [31,32].

2.3 Boundary conditions and deformation simulations

The thin film computational specimens are subsequently annealed at 600 K for a period of 0.5 ns and cooled to 300 K over another 0.5 ns in Nose-Hoover style NVT ensemble with a relaxation time of $\tau_T = 100$ fs. After that the system is relaxed in Nose-Hoover style NPT ensemble at a temperature of 300 K and pressure of 1 atmosphere, with a relaxation time of the thermostat as $\tau_T = 100$ fs and that for the barostat as $\tau_P = 200$ fs. For maintaining the film configurations, only the stress components in the horizontal directions of the film cross-section i.e. σ_{xx} and σ_{yy} should be controlled by the barostat. The stress component along the thickness directions σ_{zz} is self-equilibrated due to free boundary conditions on the surfaces.

Three types of loading in the form of deformation histories are simulated for developing the continuum constitutive model for PS thin films. These are:

- *Loading type 1:* Uniaxial straining with lateral displacement constraints by applying strain in the z -(thickness) direction, while the lateral directions (x and y) are held fixed. This is expressed in terms of the stretch ratios in the three directions as: $\lambda_z \neq 1$ and $\lambda_x = \lambda_y = 1$;

- *Loading type 2:* Uniaxial straining with lateral applied traction by applying strain in the z -(thickness) direction, i.e. $\lambda_z \neq 1$ while keeping the traction on the lateral surfaces at a constant of 1 atmosphere;
- *Loading type 3:* Tri-axial deformation by applying strains in all three directions, expressed in terms of the stretch ratios as $\lambda_x = \lambda_y = \lambda_z \neq 1$.

The three loading types are significant with respect to determination of the continuum constitutive model, and can be readily implemented in the LAMMPS code. Loading type 2 is consistent with the widely studied uniaxial material loading tests, e.g. in [27,28] and can provide validation of the model by comparison with experimental data. This loading is also significant for investigating the deviatoric deformation behavior of polymeric materials, which is dominant for incompressible or near incompressible materials. The loading type 3 corresponds to hydrostatic deformation and can be used to investigate the dilatation deformation behavior. Loading type 1 involves both deviatoric and dilatation components of deformation and can be used to validate the constitutive model after parameters have been calibrated from the results of loading types 2 and 3.

The film deformation in the thickness direction is controlled by adding two rigid walls at the top and bottom of the film. These walls are simultaneously moved at a constant velocity to provide the necessary thickness deformation. The interactions between the wall and the PS atoms are given by a potential function:

$$U_{\text{wall}}(r) = 4\varepsilon_b[(\sigma_b/r)^{12} - (\sigma_b/r)^6] \quad (2)$$

where r is the distance between the atom and the wall. The L–J cutoff radius is set to $r_c = 2^{1/6}\sigma_b$ for only including the repulsive force. Various values have been tested for the parameters ε_b and σ_b without any marked difference in the results. Thus the values are chosen as $\varepsilon_b = 0.0005$ and $\sigma_b = 3.0$ respectively. To begin the deformation process, the repulsive walls are placed beyond the interaction range of the film atoms and moved towards the film center until the forces on the walls are no longer zero. This defines the initial positions of the walls. The film thickness is measured as the distance between the two walls. Deformations in the other directions for the thin film models or for the bulk model are realized by extending or shrinking the simulation boxes in the corresponding directions. The Nose-Hoover NVT ensemble is used for simulating the loading types 1 and 3. For the loading type 2, the Nose-Hoover NPT ensemble is applied to control the stress components in the transverse directions. Since only the compressive deformation can be exerted by the rigid wall method, all simulations in this paper are for compression, i.e. $\lambda_z < 0$.

In post-processing the MD simulation results for the continuum stress–strain relations, the averaged virial stress over the current entire simulation specimen is denoted as the Cauchy stress σ . This stress involves both the kinetic energy and the interaction between atoms and can be related to the external loading on the film. While there is some controversy on whether the mechanical stress should correspond to the virial stress [37,38] or it should only involve the atomic interactions [39], the former is considered more appropriate with the MD based simulations in this work. The calculated virial stress in the z direction matches the stress calculated from the force on the repulsive atomic walls at the thin film surface very well. The stretch in the film thickness direction is calculated as $\lambda_z = H_t/H_0$, where H_0 and H_t are respectively the initial and current distances between the walls that compress the films. For the x - and y -directions with periodic boundary conditions, the stretch is calculated as $\lambda_\alpha = L_t/L_0$, $\alpha = x, y$, where L_0 and L_t are respectively the initial and current simulation box lengths in that direction. The engineering strain and the logarithmic strain along z direction are then calculated as $e_{zz} = \lambda_z - 1$ and $\varepsilon_{zz} = \ln \lambda_z$, respectively.

3 Calibrating size and rate-dependent constitutive parameters

Parameters in the continuum constitutive law are derived from homogenized solutions of a sequence of MD simulations for each simulation specimen. All simulations are carried out at 300 K with relaxation constants $\tau_T = 100$ and $\tau_P = 200$ fs respectively. Unless otherwise specified, the equations of motion are integrated with a time step of 2 fs and the engineering strain rate of the applied straining is $1 \times 10^8 \text{ s}^{-1}$.

3.1 Validation studies for a bulk specimen

Results of the MD simulation are first compared with those presented by Vorselaars et al. [27] for the uniaxial straining with lateral stresses for the load type 2 on a bulk specimen. A different united-atom MD model has been used by Vorselaars et al. [27].

The changes in stress, density, internal energy and external work during the deformation are plotted as a function of strain in Figs. 2, 3 and 4, and are compared with results in the literature. Good agreement between the present MD simulation results and those in [27] is taken as a validation of the present model. As a matter of fact, comparison of density profiles in Fig. 3 shows that the results of this analysis agrees better with experimental values [40] than those in [27].

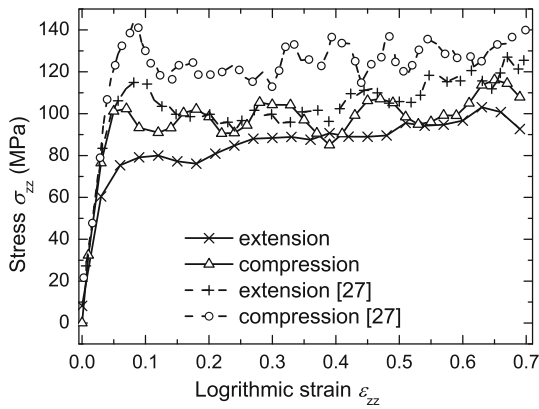


Fig. 2 Stress–logarithmic strain response by MD simulation results compared with that by Vorselaars et al. [27]

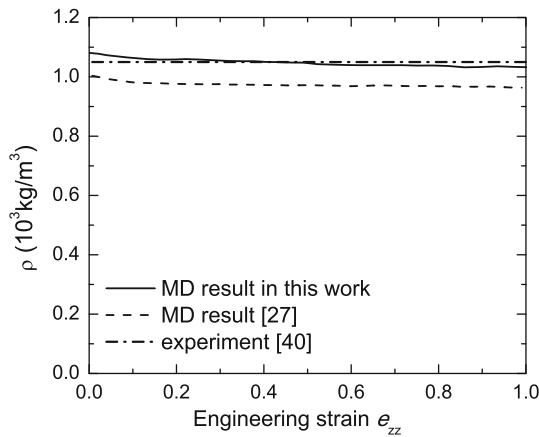


Fig. 3 Comparison of density as a function of engineering strain by MD simulation with that by Vorselaars et al. [27], as well as with the experiment value for un-deformed bulk [40]

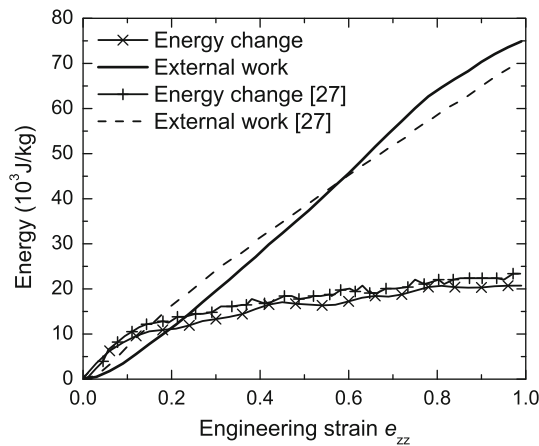


Fig. 4 Comparison of internal energy change and external work as a function of engineering strain response by MD simulation with that by Vorselaars et al. [27]

3.2 Constitutive parameters

3.2.1 A framework of elastic–plastic constitutive law for finite deformation

Since the deformation of polymeric materials usually involves large strains, an elasto-plastic finite deformation model proposed by Moran et al. [41] is applied to establish the size and rate dependent constitutive law. In this model, the deformation gradient \mathbf{F} is decomposed into an elastic part and a plastic part as:

$$\mathbf{F} = \mathbf{F}^e \cdot \mathbf{F}^p \tag{3}$$

The plastic part of the deformation gradient maps the material line element in the undeformed configuration $d\mathbf{X}$ to that in the intermediate configuration $d\bar{\mathbf{X}}$ as $d\bar{\mathbf{X}} = \mathbf{F}^p \cdot d\mathbf{X}$. The elastic deformation gradient maps the material line element $d\bar{\mathbf{X}}$ to that in the deformed configuration $d\mathbf{x}$ as: $d\mathbf{x} = \mathbf{F}^e \cdot d\bar{\mathbf{X}}$. The Green strain and its elastic and plastic corresponding parts are defined as

$$\mathbf{E} = \frac{1}{2}(\mathbf{C} - \mathbf{1}), \mathbf{E}^p = \frac{1}{2}(\mathbf{C}^p - \mathbf{1}), \bar{\mathbf{E}}^e = \frac{1}{2}(\bar{\mathbf{C}}^e - \mathbf{1}) \tag{4}$$

where $\mathbf{C} = \mathbf{F}^T \cdot \mathbf{F}$ is the right Cauchy–Green tensor and $\mathbf{C}^p = \mathbf{F}^{pT} \cdot \mathbf{F}^p$, $\bar{\mathbf{C}}^e = \mathbf{F}^{eT} \cdot \mathbf{F}^e$ are its corresponding plastic and elastic parts, respectively. Moran et al. [41] have established their constitutive law in the intermediate configuration. The stress in this formulation is expressed as:

$$\bar{\mathbf{T}} = \frac{\partial W(\bar{\mathbf{E}}^e, \theta)}{\partial \bar{\mathbf{E}}^e} \tag{5}$$

where $W(\bar{\mathbf{E}}^e, \theta)$ is the Helmholtz free energy per unit volume, usually referred to as the strain energy density, and θ is temperature. $\bar{\mathbf{T}} = \left(\mathbf{F}^e \mathbf{F}^e \right)_*^{-1} (J^e \boldsymbol{\sigma})$ is the second Piola–Kirchhoff stress in the intermediate configuration, $J^e = \det(\mathbf{F}^e)$ corresponds to the local volume change ratio during elastic deformation. Assuming that plastic deformation does not alter the local density as verified in Sect. 3.2.3, J^e corresponds to the local volume change, i.e. $J = J^e = \det(\mathbf{F})$. Under isothermal conditions, the relation between $\dot{\bar{\mathbf{T}}}$ and $\dot{\bar{\mathbf{E}}}^e$ can be deduced as

$$\dot{\bar{\mathbf{T}}} = \bar{\mathbf{D}}^e : \dot{\bar{\mathbf{E}}}^e \tag{6}$$

with $\bar{\mathbf{D}}^e = \frac{\partial^2 W(\bar{\mathbf{E}}^e, \theta)}{\partial \bar{\mathbf{E}}^e \partial \bar{\mathbf{E}}^e}$ as the elasticity tensor. For plastic deformation, the yield surface is defined as $\Phi(\bar{\mathbf{T}}, \bar{\mathbf{C}}^e, \bar{\boldsymbol{\xi}}) = 0$, where $\bar{\boldsymbol{\xi}}$ is a set of internal variables. Their evolution is governed by the hardening laws of the form $\dot{\bar{\boldsymbol{\xi}}}_\alpha = \dot{\bar{\boldsymbol{\varepsilon}}}^p H_\alpha(\bar{\mathbf{T}}, \bar{\mathbf{C}}^e, \bar{\boldsymbol{\xi}})$, $\alpha=1, 2, \dots, n$. Here $\dot{\bar{\boldsymbol{\varepsilon}}}^p$ is the rate of effective plastic strain in the intermediate configuration. Assuming associative flow rule, the plastic flow is written as

$$\dot{\bar{\mathbf{E}}}^p = \dot{\bar{\varepsilon}}^p \frac{\partial \Phi(\bar{\mathbf{T}}, \bar{\mathbf{C}}^e, \bar{\xi})}{\partial \bar{\mathbf{T}}} \quad (7)$$

The parameter $\dot{\bar{\varepsilon}}^p$ can be determined from the consistency conditions given in the Appendix Eq. (A1). The stress–strain relation is expressed as

$$\dot{\bar{\mathbf{T}}} = \bar{\mathbf{D}}^{ep} : \dot{\bar{\mathbf{E}}} \quad (8)$$

where, $\bar{\mathbf{D}}^{ep}$ is the elastic–plastic tangent tensor. Equation (8) can be written in the deformed configuration with a transformation as

$$\boldsymbol{\tau}^{(*)} = \mathbf{D}^{ep} : \mathbf{d} \quad (9)$$

where $\boldsymbol{\tau}^{(*)}$ is an objective rate of Kirchhoff stress $\boldsymbol{\tau} = J\boldsymbol{\sigma}$, \mathbf{d} is the rate of deformation tensor, \mathbf{D}^{ep} is the elastic–plastic tangent tensor in the deformed configuration. Details on the derivation and expression for $\bar{\mathbf{D}}^{ep}$ are given in Appendix A.

The explicit functions and constitutive parameters are generated from MD simulation results for the polymeric thin films in the following sections, respectively for the elastic part and plastic part of the above constitutive law. The constitutive law is aimed to investigate the size and rate dependence, which are assumed to be reflected in the calibrated constitutive parameters.

3.2.2 Hyperelastic constitutive law for the polymeric thin film

The elastic part of the finite deformation behavior of PS thin films is represented by a hyperelastic constitutive model for polymers. Hyperelastic models in the literature [42] are classified into two categories, (i) represented by a polynomial form of the energy function [43], such as the neo-Hookean model, Mooney–Rivlin model or the Arruda–Boyce 8-chain model [44], and (ii) represented by a power law, such as the Ogden model [45] and its variations [46, 47]. In the present work, the framework of the Ogden model [46] is used to represent the continuum hyperelastic constitutive law. The constitutive parameters in this model are assumed to be governed by the Hill–Mandel principle of macro-homogeneity and are generated by homogenizing results of MD simulations of the polymeric chain ensemble. The strain energy function for the power law function, which is adaptable to a variety of nonlinear stress–strain relations, is expressed as:

$$W = \sum_{p=1}^N \frac{a_p}{\alpha_p} \left(\sum_{i=1}^3 \hat{\lambda}_i^{\alpha_p} - 3 \right) + \frac{K}{m^2} (m \ln J + J^{-m} - 1) \quad (10)$$

where λ_i , $i = 1, 2, 3$ is the principal stretch, $\hat{\lambda}_i = \lambda_i^2 / J^{2/3}$ is the principal deviatoric stretch and $J = \lambda_1 \lambda_2 \lambda_3$. Coefficients a_p ($p = 1, \dots, N$) are generalized moduli, K is the bulk modulus, and α_p ($p = 1, \dots, N$) and m are exponents that can be calibrated from results of the MD simulations.

The two terms in the energy function in Eq. (10) are related to the deviatoric and volumetric parts of deformation, respectively. This partitioning is appropriate for modeling incompressible or nearly incompressible behavior, a characteristic of glassy PS deformation, as discussed by Gilmour et al. [48]. The principal components of Cauchy stress is deduced from the energy function in Eq. (10) as:

$$\begin{aligned} \sigma_i &= \frac{\lambda_i}{J} \frac{\partial W}{\partial \lambda_i} \\ &= \frac{2}{J} \sum_{p=1}^N a_p \left(\hat{\lambda}_i^{\alpha_p} - \frac{1}{3} \sum_{r=1}^3 \hat{\lambda}_r^{\alpha_p} \right) + \frac{K}{mJ} (1 - J^{-m}) \end{aligned} \quad (11)$$

The elasticity tensor for this model is given in Appendix B. For all three loading types described in Sect. 2.3, the three principal stretch directions are always in the x, y, z coordinates. Thus the principal stretches and the principal stress components are λ_i and σ_{ii} , respectively, where $i = x, y, z$ (no summation).

Utilizing the stretch constraints $\lambda_x = \lambda_y = 1$ for loading type 1, the stress–strain relation in Eq. (11) can be represented by the $\sigma_{zz} - \lambda_z$ relation as:

$$\begin{aligned} \sigma_{zz} &= \frac{4}{3\lambda_z} \sum_{p=1}^N a_p \left(\lambda_z^{4\alpha_p/3} - \lambda_z^{-2\alpha_p/3} \right) \\ &\quad + \frac{K}{m\lambda_z} (1 - \lambda_z^{-m}) \end{aligned} \quad (12)$$

For loading type 2, the stresses $\sigma_{xx} = \sigma_{yy} \approx 0$, the corresponding relation is:

$$\sigma_{zz} = \frac{2}{J} \sum_{p=1}^N a_p \left((\lambda_z/J^{1/3})^{2\alpha_p} - (\lambda_z/J^{1/3})^{-\alpha_p} \right) \quad (13)$$

On the other hand, for loading type 3 for which, $\lambda_x = \lambda_y = \lambda_z$, the relation is:

$$\sigma_{zz} = \frac{K}{m\lambda_z^3} (1 - \lambda_z^{-3m}) \quad (14)$$

Size dependence of the hyperelastic constitutive model is assumed for polymeric thin films. In this representation, the energy function in Eq. (10) is assumed to be an explicit function of the film thickness H , a parameter that is deduced from the thin film MD simulations. To explore the thickness dependence of the calibrated parameters in the energy function, the number of terms in the series N and the exponents are fixed for different specimens. Only the generalized moduli are calibrated using the following steps.

- i. The bulk modulus K is calibrated according to Eq. (14) from the $\sigma_{zz} - e_{zz}$ curves of loading type 3.
- ii. The generalized moduli related to the deviatoric deformation parameters a_p , ($p = 1, \dots, N$) in Eq. (13) are calibrated from the $\sigma_{zz} - e_{zz}$ curves for loading type 2. In this phase, only the elastic part of the curves is fitted. The elastic range is determined from the yield point near the onset of the zero slope in the stress–strain curve.
- iii. The constitutive model is validated by comparing the function of Eq. (12) with the calibrated parameters for results of MD simulations under loading type 1.

Figures 5a–c show the stress–strain plots for films of different thicknesses for the three types of applied loading and deformation respectively. Results for the thin films are also compared with the bulk response in these plots. Unless otherwise specified, only the magnitudes of respective stresses and strains are plotted in these figures. For the different loadings considered the slope of the stress–strain plot decreases with diminishing film thickness. This signifies considerable reduction in the material stiffness. The stress responses for the constrained uniaxial straining of loading type 1 and triaxial straining of loading type 3 are orders of magnitude larger in comparison with those for uniaxial straining with lateral applied stresses for loading type 2. This difference may be attributed to the large volume change and the associated hydrostatic stresses for the loadings of type 1 and 3. As seen in Fig. 6, the volume change in a 22.6 nm thick film is approximately 4% for an engineering strain ϵ_{zz} of 30% for the loading type 2, while the corresponding volume changes are 30% for loading 1 and 66% for loading type 3. These results indicate that the stress is much larger for volumetric deformation than for deviatoric deformation for PS. Figure 6 also shows that the volume stops decreasing after a certain amount of straining for loading type 2, while it decreases continuously for loading type 1. This is consistent with the change in hydrostatic stress, which ceases to increase beyond a certain value for loading type 2 but keeps increasing for loading type 1. Also, yielding restrains further increase in the deviatoric stress after a threshold strain is attained for loading type 2. As discussed in the next section, this explains why the stresses stop increasing with strain for the loading type 2 in Fig. 5b, while they continuously increase for loading type 1 in Fig. 5a.

The calibrated parameters are listed in Table 1. Here the fixed parameter values are chosen from Ref. [49] as $N = 3, m = 5$ and $\alpha_p = 0.65, 2.5, -1$ respectively for $p = 1, 2, 3$. The data shows that the bulk modulus K is much larger than other moduli a_p ($p = 1, 2, 3$). This indicates that PS has a much stiffer response to volumetric strains in comparison with deviatoric strains. Thus for the constrained

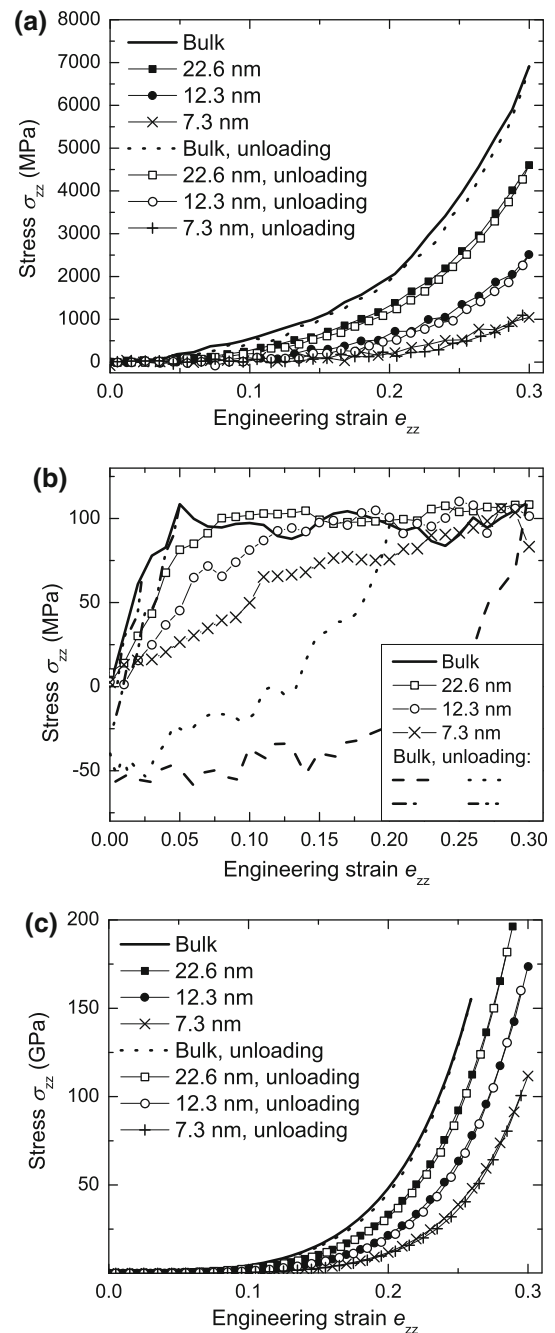


Fig. 5 Stress–strain plots for simulation specimens of different film thicknesses as well as for bulk response, under: (a) constrained uniaxial straining (loading type 1); (b) uniaxial straining with lateral stresses (loading type 2); (c) triaxial straining (loading type 3). All deformations shown are for compression

uniaxial straining of loading type 1, which involves both deviatoric and dilatation strains, stresses from the bulk deformation dominate over that from the deviatoric component of deformation.

Table 1 Bulk modulus K and parameters a_i ($i = 1, 2, 3$) calibrated from stress–strain curves generated from MD simulations for different systems

Thickness (nm)	Chains \times monomers	K (GPa)	a_1 (MPa)	a_2 (MPa)	a_3 (MPa)
5.2	5×200	0.134	34.1	1.18	−0.848
7.3	10×200	0.621	103	2.51	−3.20
12.3	20×200	1.55	225	5.28	−6.58
17.3	30×200	2.17	321	7.35	−8.84
22.6	40×200	2.60	396	9.06	−10.4
Bulk	8×320	4.38	754	17.5	−18.6

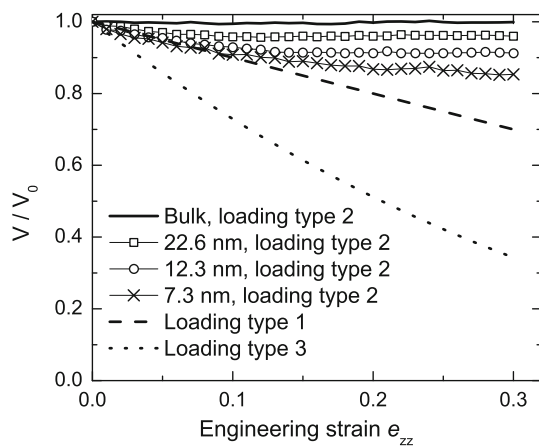


Fig. 6 Volume change for different film thicknesses and for bulk behavior under loading types 1–3

3.2.3 Effective plastic yielding in the PS response

Figure 5b shows considerable difference in loading-unloading behavior of PS under uniaxial straining. This difference is however significantly lower for dilatation dominated deformation cases of loading types 1 and 3, as shown in Fig. 5a and c. The volumetric part of the deformation is predominantly elastic, whereas plastic yielding is observed for deviatoric deformation of loading type 2. Comparison of the stress–strain and volume change behavior reveals that the condition of yielding in Fig. 5b is consistent with the regime where further volume change ceases in Fig. 6. Plasticity in the deformation of PS has been reported by Vorselaars et al. [27]. The yield stress σ_y in this analysis is determined from the onset of near-zero slopes in the stress–strain curves of type 2 loading in Fig. 5b. The stress response from the MD simulations is found to stabilize into a plateau beyond this point. The yield point is ascertained by comparing the loading

and unloading curves of bulk for different maximum loading stresses. The yield stress is found to be approximately 100 MPa for the bulk PS specimen, as well as for films of different thicknesses. The unloading curves are close to the loading curve if the maximum loading stress is lower than 100 MPa for the bulk specimen. Figure 5b also shows that the stress remains around 100 MPa after yielding. Thus the behavior of PS may be assumed to be represented well by a perfect plasticity model. The corresponding yield condition is given as:

$$\Phi = \sigma_{\text{eq}} - \sigma_y(h, \dot{\epsilon}) = 0 \quad (15)$$

where $\sigma_{\text{eq}} = \sqrt{\frac{2}{3} \boldsymbol{\sigma}' : \boldsymbol{\sigma}'}$ is the equivalent stress, $\boldsymbol{\sigma}'$ is the deviatoric stress tensor, σ_y is the yield stress which is a function of the film thickness and strain rate only. From the above MD simulation results, $\sigma_y = 100 \text{ MPa}$ for an applied strain rate $\dot{\epsilon}_{zz} = 10^8 \text{ s}^{-1}$. No significant size dependence is observed for this behavior. Thus the plastic part of constitutive law is expressed as

$$\mathbf{d}^p = \dot{\epsilon}^p \mathbf{n} \quad (16)$$

where, \mathbf{d}^p is the plastic deformation rate tensor, $\mathbf{n} = \frac{3\boldsymbol{\sigma}'}{2\sigma_{\text{eq}}}$ is the normalized flow direction and $\dot{\epsilon}^p$ is the equivalent plastic strain rate in the deformed configuration.

3.2.4 Validation by the constrained uniaxial straining

The constitutive model for general finite deformation of PS combines the elastic and plastic descriptions in Sects. 3.2.2 and 3.2.4, respectively. Details of derivations are given in the Appendix C with the overall expressions in Eqs. (C9–C11). In this section, the simple loading type 1 of constrained uniaxial straining is used for validating the calibrated constitutive parameters. Combining Eqs. (12) and (15), the $\sigma_{zz} - \lambda_z$ relation is expressed as:

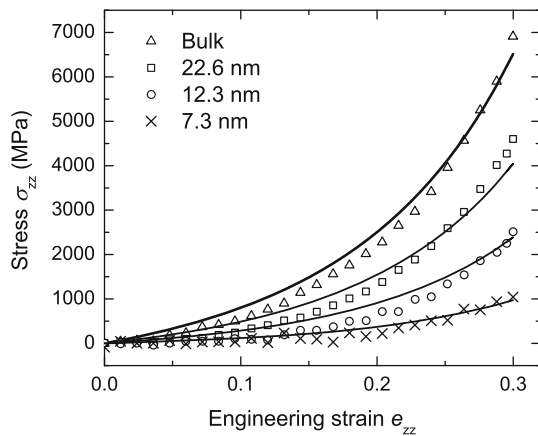


Fig. 7 Stress–strain plots from the calibrated hyperelastic model (solid lines) with those from the MD simulation results (discrete points) for films of different thicknesses and the bulk specimen under loading type I

$$\sigma_{zz} = \begin{cases} \frac{4}{3\lambda_z} \sum_{p=1}^N a_p \left(\lambda_z^{4\alpha_p/3} - \lambda_z^{-2\alpha_p/3} \right) + \frac{K}{m\lambda_z} (1 - \lambda_z^{-m}), & \forall \frac{2}{\lambda_z} \sum_{p=1}^N a_p \left(\lambda_z^{4\alpha_p/3} - \lambda_z^{-2\alpha_p/3} \right) \leq \sigma_y \\ \frac{2}{3}\sigma_y + \frac{K}{m\lambda_z} (1 - \lambda_z^{-m}), & \forall \frac{2}{\lambda_z} \sum_{p=1}^N a_p \left(\lambda_z^{4\alpha_p/3} - \lambda_z^{-2\alpha_p/3} \right) > \sigma_y \end{cases} \quad (17)$$

Figure 7 compares the stress–strain plots by the calibrated constitutive model with the MD simulation results. The consistency of the compared results validates the robustness of the size-dependent constitutive model.

3.3 Size dependence of the constitutive parameters

The MD simulation results in Sect. 3.2 exhibit size dependence of the calibrated parameters in the material constitutive law for films of different thicknesses. The distribution of local material parameters across the film thickness is further investigated in this section using these results. Since the yield stress and post-yielding stress in PS do not vary significantly with film thickness in the MD simulations, size dependence in this study is restricted to the generalized moduli K and parameters a_i ($i = 1, 2, 3$) in the hyperelastic model. Due to ambiguity in the definition of local stresses and strains in MD for thin film models, it is impossible to directly obtain the local material law from the local stress–strain response. Additionally, the film cannot be divided into layers in the thickness direction to determine the material properties of each layer due to local diffusion. To alleviate these limitations, the following method is proposed to generate distribution functions of local properties along the film thickness.

An assumption is made that the free standing films have symmetric properties about the mid-plane and that the average property of the film section from the surface to a depth $H/2$ corresponds to that of a film of thickness H , consistent

with observations in [4]. Accordingly, the averaged material parameter for a film of thickness H may be expressed as:

$$\bar{M}(H) = \frac{2}{H} \int_0^{H/2} M(h)dh \quad (18)$$

$\bar{M}(H)$ represents the generalized moduli including the bulk modulus K and parameters a_i ($i = 1, 2, 3$) for a film of thickness H , and $M(h)$ represents the corresponding local values at a depth h from the surface. The thicknesses of the computer simulated specimens are given by discrete values $H_1, H_2, \dots, H_n; \forall H_1 < H_2 < \dots < H_n$ with small increments $\Delta H_i = H_i - H_{i-1}$. Equation (18) can be rewritten in a discrete form as:

$$\bar{M}(H_m) = \frac{1}{H_m} \sum_{i=1}^m M(h_i)(H_i - H_{i-1}) \quad (19)$$

where $\bar{h}_i = (H_i + H_{i-1})/4$. The variation of $M(h)$ can be determined from $\bar{M}(H_i)$ ($i = 1, \dots, n$) as:

$$M(\bar{h}_i) = \frac{\bar{M}(H_i)H_i - \bar{M}(H_{i-1})H_{i-1}}{H_i - H_{i-1}} \quad (20)$$

Figure 8a–d plot the deduced local material parameters as a function of distance from the free surface for the four generalized moduli a_1, a_2, a_3 and K , respectively. The figures also compare the specimen material parameters of different films as a function of film thickness. All results for the overall material parameters show a similar trend, i.e. the data converge to their bulk values as the film thickness increases, or as the distance from surface increases for the local material parameters. To exhibit this trend clearly, the local material parameters are plotted as a normalized function $M_{\text{norm}} = -\ln(1 - M/M_{\text{bulk}})$ in Fig. 9. Here M_{bulk} is the corresponding value for the bulk specimen. The graph shows nearly linear relations between M_{norm} and h . This indicates that the distribution of the local modulus across the film thickness follows the relation:

$$M(h) = M_{\text{bulk}} \left(1 - e^{-(h-h_0)/h_\tau} \right) \quad (21)$$

where parameter h_0 can be thought of as the surface layer thickness and h_τ is a characteristic decay depth of the surface influence into the film. The calibrated parameters are listed in Table 2, with h_0 approximately 1 nm and h_τ

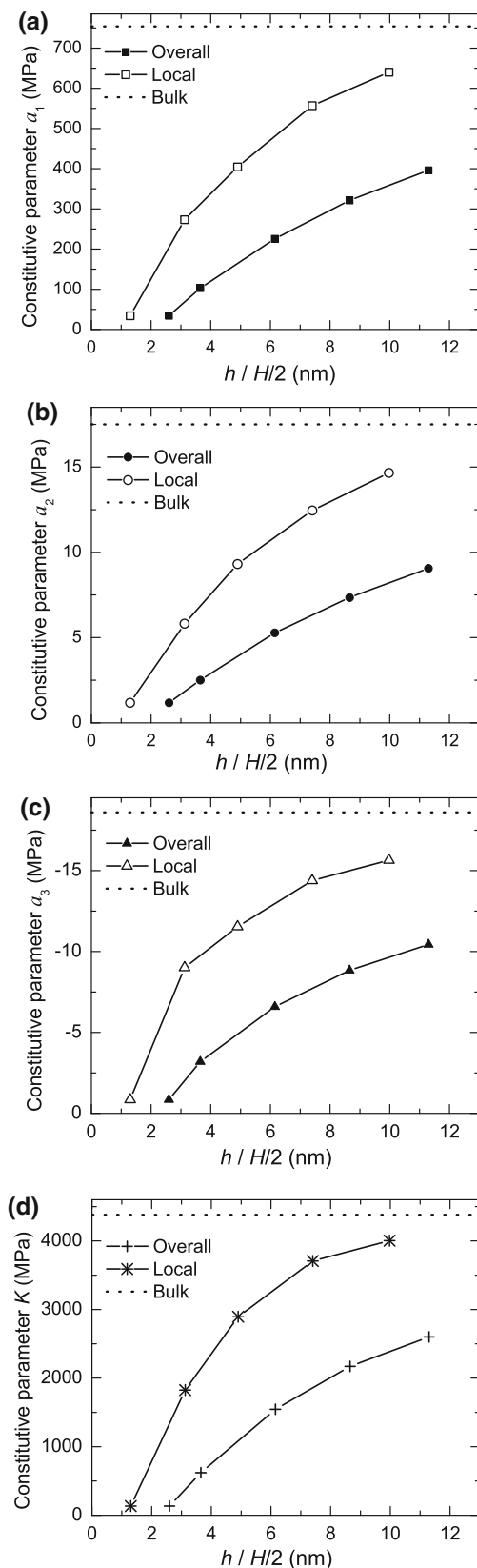


Fig. 8 Local and overall material parameters as a function of the distance from the surface h (or different film thicknesses H) for: (a) a_1 , (b) a_2 , (c) a_3 , (d) K , respectively

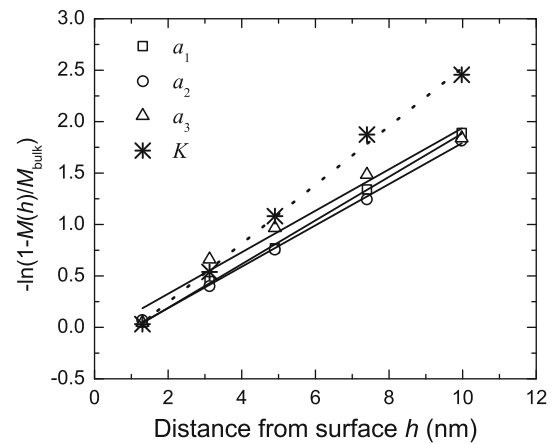


Fig. 9 Normalized local material parameters as a function of the distance along PS film thickness. Lines are formed by linear fitting of the computational data

approximately 5 nm. Using Eq. (21), the generalized moduli for a film of thickness H can be written as:

$$\bar{M}(H) = M_{\text{bulk}} \left[1 - \frac{2h\tau}{H} e^{h_0/h\tau} \left(1 - e^{-H/2h_0} \right) \right] \quad (22)$$

3.4 Rate dependence of constitutive parameters

Rate effects are observed in the MD simulations of the PS model and are incorporated in the constitutive law. Different values of engineering strain rates $\dot{\epsilon}_{zz}$ from 1×10^6 to $1 \times 10^9 \text{ s}^{-1}$ are applied to the MD model of PS for simulating the overall deformation patterns. MD simulations for lower strain rate values are very time consuming. It takes $\sim 6,000$ CPU hours on an IBM Cluster 1350, dual socket, dual core 2.6 GHz Opteron to simulate bulk deformation of a molecular specimen to an engineering strain of 0.3 under a strain rate of $1 \times 10^6 \text{ s}^{-1}$ with a time step of $4fs$. Consequently, simulations for exploring rate effects are carried out with a single bulk specimen. Figure 10a and b show the stress–strain plots for the uniaxial straining with lateral 1 atmosphere pressure in loading type 2, and triaxial straining of loading type 3, respectively. In Fig. 10a, the rate effect is very significant with a larger stress response for a higher strain rate. However, for loading type 3, the stress–strain plots do not exhibit any rate dependence. These results indicate that rate effect is important for the deviatoric component of deformation, while the volumetric part is relatively rate independent.

Figure 10a demonstrates that the constitutive parameters that are dependent on the strain rate $\dot{\epsilon}_{zz}$ include the generalized moduli related to deviatoric deformation parameters a_p , ($p = 1, 2, 3$) and the yield stress σ_y . Parameters a_p can be calibrated in accordance with Eq. (13) from the elastic part of the stress–strain curves in Fig. 10a. The yield stress σ_y , on the other hand, can be determined from the onset of near-zero slopes in those curves. The calibrated constitutive parameters

Table 2 Calibrated parameters for the distribution of local moduli

Modulus	h_τ (nm)	h_0 (nm)	R^2 Value for least square minimization
a_1	4.71	1.10	0.998
a_2	4.98	1.07	0.998
a_3	4.96	0.38	0.967
K	3.51	1.14	0.995

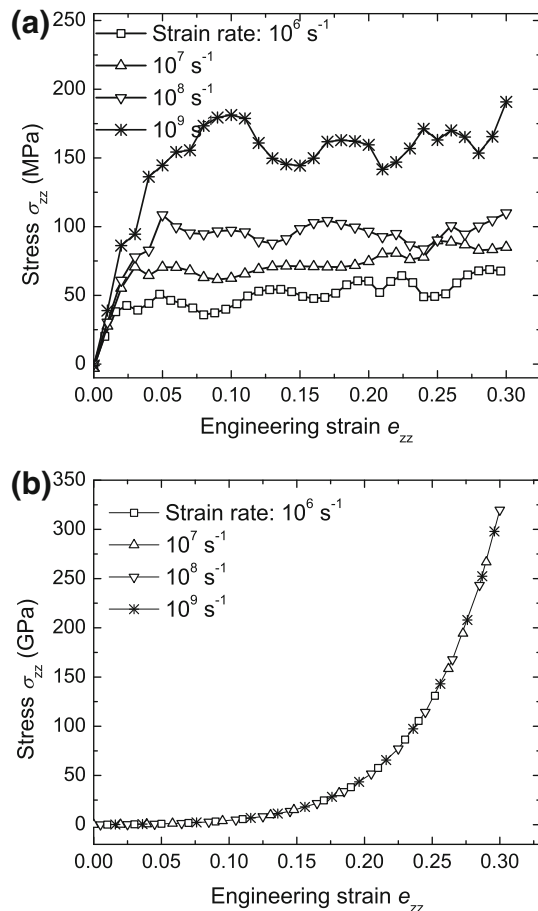


Fig. 10 Stress–strain plots for: (a) uniaxial straining of loading type 2 with lateral 1 atmosphere pressure, and (b) triaxial straining of loading type 3 under different strain rates, for the bulk specimen

are plotted as a function of the engineering strain rate $\dot{\epsilon}_{zz}$ in Fig. 11. As can be seen, the data points for each constitutive parameter are almost linear in the log–log plot. This indicates a power law dependence of the constitutive parameters on strain rate, expressed as:

$$M = M_0 \dot{\epsilon}_{zz}^m \tag{23}$$

where M represents the respective constitutive parameters a_p , ($p = 1, 2, 3$) and σ_y , M_0 is a constant with the same unit as M , m is the index of the power function dependence.

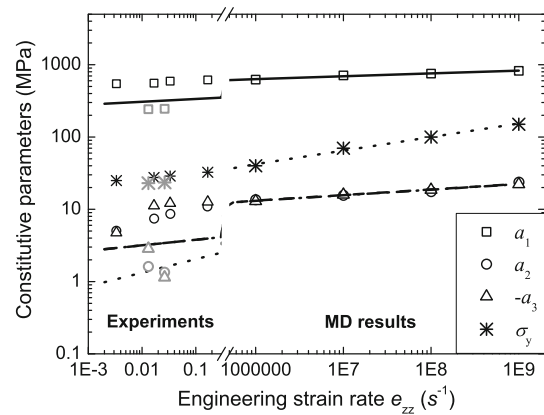


Fig. 11 Constitutive parameters as a function of the engineering strain rate for PS bulk specimen on a log–log scale. The lines are generated from linear fitting. The symbols in the fast rate region are calibrated from MD simulation results while those in the slow rate region are from experiments in [50]. Black and grey colors correspond to two measuring methods

and M_0 are determined from the slope and interception of the linear fit for each constitutive parameter in Fig. 11, as listed in Table 3. The calibrated constitutive parameters from the experiments in [50] are also compared in Fig. 11. It is seen that the experimental data lie near the linear fitted lines for the generalized moduli a_p , ($p = 1, 2, 3$). This supports the ability of Eq. (23) in predicting the rate dependence of constitutive parameters across a large range of strain rates. For the yield stress σ_y , however, the calibrated function of Eq. (23) from simulation results is not able to predict the experimental data well. The rate dependence law Eq. (23) is deduced from MD results with strain rates $\dot{\epsilon}_{zz}$ in the range 1×10^6 to $1 \times 10^9 \text{ s}^{-1}$, and is only valid for a certain range of strain rates. It should be noted that it is not applicable when the strain rate tends to zero because in that case the stress will also tends to zero. The yield stress discrepancy may point to the fact that the dominating mechanisms of yield at the experimental strain rates are different from those manifested in the MD simulation strain rates.

In the MD simulations for loading type 2, $\dot{\epsilon}_{zz}$ is not much different from the equivalent strain rate $\dot{\epsilon} = \sqrt{\frac{2}{3}} \mathbf{d} : \mathbf{d}$. Thus Eq. (23) may be written in a more generalized form as

Table 3 Calibrated constants for power law rate dependence for bulk PS

M	M_0 (MPa)	m	R^2 value for least square minimization
a_1	368	0.039	0.960
a_2	4.53	0.077	0.919
a_3	4.52	0.077	0.995
σ_y	3.15	0.190	0.986

$$M(\dot{\varepsilon}) = M_0 \dot{\varepsilon}^m \quad (24)$$

3.5 Summary of size and rate dependence of constitutive parameters

The proposed constitutive model requires determination of five constitutive parameters in this work. They include the generalized moduli related to deviatoric deformation a_p , ($p = 1, 2, 3$), the bulk modulus K , and the yield stress σ_y . It has been concluded that K is only size dependent, σ_y is rate dependent and a_p are both size and rate dependent. Combining Eqs. (21) and (24) yields a size and rate dependent form for each constitutive parameter as

$$a_p(h, \dot{\varepsilon}) = a_{p0} \dot{\varepsilon}^m \left(1 - e^{-(h-h_0)/h_\tau}\right), \quad (p = 1, 2, 3) \quad (25a)$$

$$K(h, \dot{\varepsilon}) = K_0 \left(1 - e^{-(h-h_0)/h_\tau}\right) \quad (25b)$$

$$\sigma_y(h, \dot{\varepsilon}) = \sigma_{y0} \dot{\varepsilon}^m \quad (25c)$$

The parameter values are given in Tables 2 and 3. The size and rate dependent constitutive law is well established in this manner.

4 Discussions on size dependent behavior

MD simulation results show strong evidence of size dependence in the stress–strain relations of PS thin films. This paper develops size and rate dependent constitutive laws for PS thin films of varying thicknesses. The change in the local density distribution of molecular ensembles in MD simulations can also provide insight into the size dependence, as shown in Figs. 12 and 13. These figures plot the local density profile across the thickness at zero strain and at an engineering strain of 0.3 for thin films under constrained uniaxial straining load. They also compare the responses of the thin films and the bulk. In Fig. 12, the local density does not change much in the core region for different films, but reduces sharply near the surface. With deformation, the local density increases in the core region for the thicker films, but remains nearly unchanged for the thinner films as shown in Fig. 13. From the density distribution profile, the effective film thickness may be defined as the distance between the two positions, for which the local density corresponds to the median value of those at the core region and the outermost surface. An alternative way to define the effective thickness is to calculate the distance between the two van der Waals surfaces. The position of the van der Waals surface profile is calculated as the averaged z -coordinate location in a fine resolution grid ($\sim 3 \text{ \AA}$ in this study) on that surface. Figure 14 plots the effective thicknesses according to the two definitions, as well as the wall distance during deformation. All values are normalized with respect to the initial wall distance for each film.

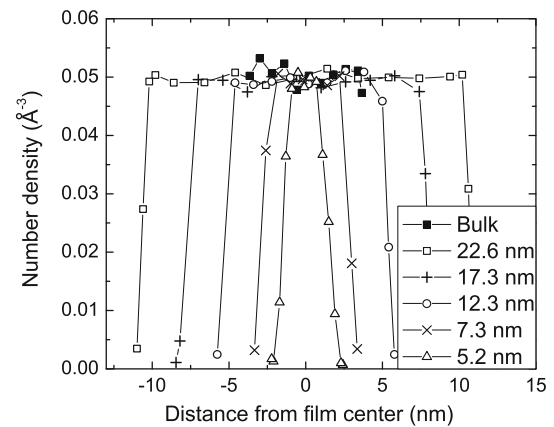


Fig. 12 Local density distribution across the thickness in stress-free state for films of different thicknesses, compared with the bulk specimen

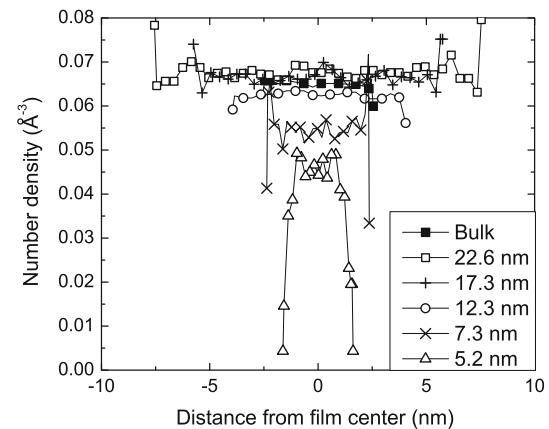


Fig. 13 Local density distribution across the thickness at stretch of $\lambda_z = 0.7$ under constrained uniaxial straining for films of different thicknesses, compared with the bulk specimen

The effective thicknesses according to the two definitions do not differ too much. Figure 14 also shows that the effective thickness changes much less for the thinner film. Figure 15 compares the normalized effective thickness defined by van der Waals surfaces for films of different thicknesses before and after uniaxial straining. Also compared is the roughness of the film surface. This is calculated as the standard deviation of the z coordinates over the grid on the van der Waals surfaces. It shows that the relative difference between the effective thickness and thickness from the wall distance is larger for the thinner film.

These results reveal that the PS thin films may be considered as a laminate of relatively softer surface layers and a harder core region. Deformation is more localized to the surface layer for thinner films. The thickness of the surface layer can be measured from the region where the local den-

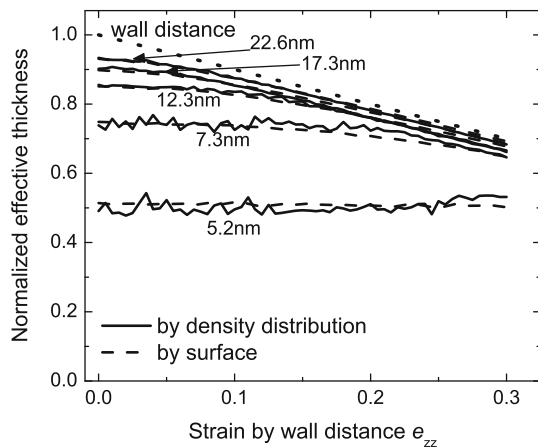


Fig. 14 Change of the effective thickness (normalized by the initial wall distance) under uniaxial straining for films of different thicknesses. Dotted line corresponds to the normalized wall distance

sity deviates from the core, as shown in Fig. 12, or reflected by the variance of the surface profile, as shown in Fig. 15. This is of order of magnitude of 1 nm, consistent with h_0 in Table 2. The width of the surface layer is not much different for different film thicknesses. It is even larger for the thinner films, rendering a larger percentage of the surface layer for the thinner film. This observation helps explain why thinner films have a lower density and stiffness. Indeed, if only the core region is considered by plotting the stress versus the relative change of density of the core region under uniaxial straining, the size dependent behavior disappears, as shown in Fig. 16. This result provides evidence that size dependence evolves from the effects at the film surface. With a smaller density near the surface, the free volume is larger, and the atomic motion is less constrained. Figure 17 shows that the mean-squared displacement (MSD) is larger for the thinner film. This observation has also been reported in the literature [51]. Figure 18 shows a higher MSD near the film surface.

5 Conclusions

The mechanical properties of PS thin films are investigated by the MD simulations in this paper. The simulations not only show the size and rate dependent properties of these films but also reveal some insights for the size dependence from an atomic viewpoint. A size-dependent and rate-dependent continuum scale constitutive law is established based on these simulations. The model establishes rate and size dependent parameters in a hyperelastic constitutive framework. Post yield behavior is found to be essentially perfectly plastic with a rate dependent yield strength. Continuum simulations can be carried out on a large scale for better understanding the experiments such as nanoindentation and nanoparticle embedding on polymer thin films that are used

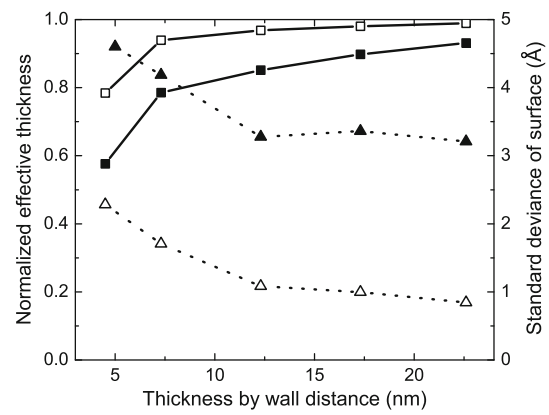


Fig. 15 Distance between the van der Waals surfaces normalized by wall distance (square markers), and the standard deviation of the surface (triangle markers) versus the film thickness calculated from wall distance. Solid and hollow markers correspond to situations before and after uniaxial, straining respectively

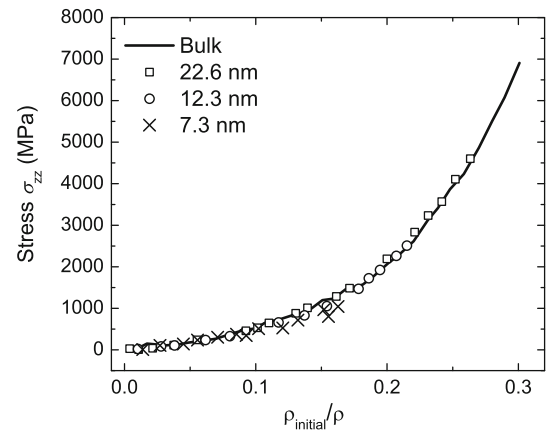


Fig. 16 Stress as a function of relative density change at the core region calculated as $\rho_{\text{initial}}/\rho$ under constrained uniaxial straining

in renewable energy applications for generation, transmission and storage of energy.

Acknowledgments This work was supported by the NSF Division of Engineering Education & Centers through grant EEC-0914790 to the Nanoscale Science and Engineering Center for Affordable Nano-engineering of Polymeric Biomedical Devices (CANPBD) at the Ohio State University. Computer support by the Ohio Supercomputer Center through grant PAS0191 is also gratefully acknowledged.

Appendix A

Detailed derivations for the expression of $\bar{\mathbf{D}}^{ep}$ in Sect. 3.2.1 are given as follows. From the yield condition $\Phi(\bar{\mathbf{T}}, \bar{\mathbf{C}}^e, \bar{\xi}) = 0$ and $\dot{\xi}_\alpha = \dot{\epsilon}^p H_\alpha(\bar{\mathbf{T}}, \bar{\mathbf{C}}^e, \bar{\xi})$, $\alpha = 1, 2, \dots, n$, the consistency condition can be written as

$$\frac{\partial \Phi}{\partial \bar{\mathbf{T}}} : \dot{\bar{\mathbf{T}}} + 2 \frac{\partial \Phi}{\partial \bar{\mathbf{C}}^e} : \dot{\bar{\mathbf{C}}}^e + \dot{\epsilon}^p \sum_\alpha \frac{\partial \Phi}{\partial \bar{\xi}_\alpha} H_\alpha = 0 \tag{A1}$$

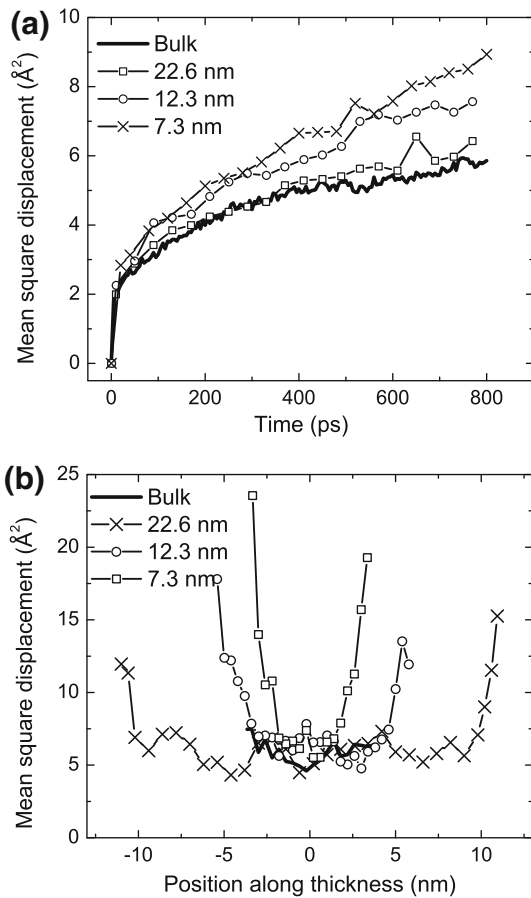


Fig. 17 (a) MSD for NVT simulations of 800 ps for films of different thicknesses and the bulk specimen; (b) distribution of MSD across the thickness for films of different thicknesses compared with the bulk

Noting that

$$\dot{\bar{\mathbf{E}}}^e = \bar{\mathbf{D}}^e = \bar{\mathbf{D}} - \bar{\mathbf{D}}^p \tag{A2}$$

and utilizing Eqs. (6–7), $\dot{\bar{\mathbf{E}}}^p$ can be obtained from Eq. (A1) as

$$\dot{\bar{\mathbf{E}}}^p = \frac{\left(\frac{\partial \Phi}{\partial \bar{\mathbf{T}}} : \bar{\mathbf{D}}^e + 2 \frac{\partial \Phi}{\partial \bar{\mathbf{C}}^e}\right) : \bar{\mathbf{D}}}{\left(\frac{\partial \Phi}{\partial \bar{\mathbf{T}}} : \bar{\mathbf{D}}^e + 2 \frac{\partial \Phi}{\partial \bar{\mathbf{C}}^e}\right) : \frac{\partial \Phi}{\partial \bar{\mathbf{T}}} - \sum_{\alpha} \frac{\partial \Phi}{\partial \xi_{\alpha}} H_{\alpha}} \tag{A3}$$

Substituting Eq. (A3) into Eq. (7) and Eq. (7) into Eq. (6), and noting Eq. (A2), the elastic–plastic tangent tensor is obtained as

$$\bar{\mathbf{D}}^{ep} = \bar{\mathbf{D}}^e - \frac{\left(\frac{\partial \Phi}{\partial \bar{\mathbf{T}}} : \bar{\mathbf{D}}^e\right) \left(\frac{\partial \Phi}{\partial \bar{\mathbf{T}}} : \bar{\mathbf{D}}^e + 2 \frac{\partial \Phi}{\partial \bar{\mathbf{C}}^e}\right)}{\left(\frac{\partial \Phi}{\partial \bar{\mathbf{T}}} : \bar{\mathbf{D}}^e + 2 \frac{\partial \Phi}{\partial \bar{\mathbf{C}}^e}\right) : \frac{\partial \Phi}{\partial \bar{\mathbf{T}}} - \sum_{\alpha} \frac{\partial \Phi}{\partial \xi_{\alpha}} H_{\alpha}} \tag{A4}$$

Pushing forward Eq. (8) into the deformed configuration with the assumption that $J^e = J$, yields the relation

$$\boldsymbol{\tau}^{\text{Oldr}(e)} = \mathbf{D}^{ep} : \mathbf{d}, \tag{A5}$$

where $\boldsymbol{\tau}^{\text{Oldr}(e)} = \dot{\boldsymbol{\tau}} - \boldsymbol{l}^e \cdot \boldsymbol{\tau} - \boldsymbol{\tau} \cdot \boldsymbol{l}^{eT}$ is the Oldroyd derivative of $\boldsymbol{\tau}$, $\boldsymbol{l}^e = \dot{\mathbf{F}}^e \cdot \mathbf{F}^{e-1}$ is the elastic velocity gradient, $\mathbf{d} = \left(\mathbf{F}^{eT} \mathbf{F}^e\right)^* \dot{\mathbf{E}}, \mathbf{D}^{ep} = \left(\mathbf{F}^e \mathbf{F}^e \mathbf{F}^e \mathbf{F}^e\right)^* \bar{\mathbf{D}}^{ep}$.

Appendix B

The strain energy for the Ogden hyperelastic model adopted in this paper can be rewritten as

$$W = \hat{W}(\hat{\lambda}_i) + h(J^e), \tag{B1}$$

where $\hat{W}(\hat{\lambda}_i) = \sum_{p=1}^N \frac{a_p}{\alpha_p} \left(\sum_{i=1}^3 \hat{\lambda}_i^{\alpha_p} - 3\right)$ and $h(J^e) = \frac{K}{m^2} (m \ln J^e + (J^e)^{-m} - 1)$. Summation convention does not apply in this and the subsequent equations. Using Eqs. (5–6), the expressions for the second P–K stress $\bar{\mathbf{T}}$ and the elasticity tensor $\bar{\mathbf{D}}^e$ in the intermediate configuration can be incarnated as (see [46]).

$$\bar{\mathbf{T}} = (J^e)^{-2/3} \hat{\mathbf{T}} + f(\hat{\lambda}_i) \bar{\mathbf{C}}^e + h' J^e \bar{\mathbf{C}}^e, \tag{B2}$$

where $\hat{\mathbf{T}} = 2 \sum_{i=1}^3 \hat{W}_{,i} \mathbf{N} \mathbf{N}$ and \mathbf{N} is the eigen-direction of $\bar{\mathbf{C}}^e$,

$$f(\hat{\lambda}_i) = -\frac{2}{3} \sum_{i=1}^3 \hat{\lambda}_i \hat{W}_{,i}, \hat{W}_{,i} = \sum_{p=1}^N a_p \hat{\lambda}_i^{\alpha_p - 1}.$$

$$\begin{aligned} \bar{\mathbf{D}}^e &= (J^e)^{-2/3} \mathbf{D} \hat{\mathbf{T}} - (h' J^e + f(\hat{\lambda}_i)) \bar{\mathbf{P}} \\ &\quad + (h' J^e + h'' (J^e)^2) \bar{\mathbf{C}}^e \bar{\mathbf{C}}^e \\ &\quad - \frac{2}{3} (J^e)^{-4/3} \hat{\mathbf{T}} \bar{\mathbf{C}}^e + 2 (J^e)^{-4/3} \bar{\mathbf{C}}^e \text{dev}(\mathbf{M}), \end{aligned} \tag{B3}$$

where $\mathbf{D} \hat{\mathbf{T}} = \frac{\partial \hat{\mathbf{T}}}{\partial \bar{\mathbf{C}}^e}$, $\bar{P}_{ijkl} = \bar{C}_{ik}^e \bar{C}_{jl}^e + \bar{C}_{il}^e \bar{C}_{jk}^e$, $\mathbf{M} = \frac{\partial f(\hat{\lambda}_i)}{\partial \bar{\mathbf{C}}^e} = -\frac{4}{3} \sum_{i=1}^3 \sum_{p=1}^N a_p \hat{\lambda}_i^{\alpha_p - 1} \mathbf{N} \mathbf{N}$, $\text{dev}(\mathbf{M}) = \mathbf{M} - \frac{1}{3} (\mathbf{M} : \bar{\mathbf{C}}^e) \bar{\mathbf{C}}^e$.

Pushing forward Eq. (B3) into the deformed configuration yields

$$\begin{aligned} (J^e \boldsymbol{\sigma})^{\text{Oldr}(e)} &= J^e \dot{\boldsymbol{\sigma}} + J^e \boldsymbol{\sigma} \text{trd}^e - \boldsymbol{l}^e \cdot (J^e \boldsymbol{\sigma}) \\ &\quad - (J^e \boldsymbol{\sigma}) \cdot \boldsymbol{l}^{eT} = \mathbf{D}^e : \mathbf{d}^e \end{aligned} \tag{B4}$$

$\mathbf{D}^e = \left(\mathbf{F}^e \mathbf{F}^e \mathbf{F}^e \mathbf{F}^e\right)^* \bar{\mathbf{D}}^e$ is the elasticity tensor in the deformed

configuration, $\mathbf{d}^e = \left(\mathbf{F}^{eT} \mathbf{F}^e\right)^* \dot{\bar{\mathbf{E}}}^e = \text{sym}(\boldsymbol{l}^e)$ is the elastic deformation rate tensor, $(J^e \boldsymbol{\sigma})^{\text{Oldr}(e)} = (J^e \boldsymbol{\sigma})' - \boldsymbol{l}^e \cdot (J^e \boldsymbol{\sigma}) - (J^e \boldsymbol{\sigma}) \cdot \boldsymbol{l}^{eT}$ is elastic Oldroyd derivative of $J^e \boldsymbol{\sigma}$. Assuming $J^e = J$, Eq. (B4) can be transformed into

$$\boldsymbol{\sigma}^{(e)\nabla} = \left(\frac{1}{J} \mathbf{D}^e + \mathbf{G}^{\sigma} - \boldsymbol{\sigma} \mathbf{1}\right) : \mathbf{d}^e, \tag{B5}$$

where $\overset{\nabla}{\sigma}^{(e)} = \dot{\sigma} - \mathbf{w}^e \cdot \sigma + \sigma \cdot \mathbf{w}^e$ is the elastic Jaumann derivative of σ and $\mathbf{w}^e = \mathbf{l}^e - \mathbf{d}^e$ is the elastic spin rate, $\mathbf{G}_{ijkl}^\sigma = \frac{1}{2} (\sigma_{ik}\delta_{jl} + \sigma_{il}\delta_{jk} + \sigma_{jk}\delta_{il} + \sigma_{jl}\delta_{ik})$.

Appendix C

The constitutive law for a perfect plastic model, adopted in this paper, is conceived as follows. To determine the plastic flow direction in Eq. (7), the expression of σ_{eq} in Eq. (15) is transformed as

$$\sigma_{eq} = \frac{1}{J^e} \left[\frac{3}{2} \text{tr} (\bar{\mathbf{C}}^e \cdot \bar{\mathbf{T}}^* \cdot \bar{\mathbf{C}}^e \cdot \bar{\mathbf{T}}^*) \right]^{1/2}, \tag{C1}$$

where $\bar{\mathbf{T}}^* = \bar{\mathbf{T}} - \frac{1}{3}(\bar{\mathbf{T}} : \bar{\mathbf{C}}^e) \bar{\mathbf{C}}^e$. Taking the derivative of Eq. (C1) and assuming $J^e = J$ results in the relation

$$J^2 \sigma_{eq} d\sigma_{eq} = \frac{3}{2} [(\bar{\mathbf{C}}^e \cdot \bar{\mathbf{T}}^* \cdot \bar{\mathbf{C}}^e) : d\bar{\mathbf{T}}^* + (\bar{\mathbf{T}}^* \cdot \bar{\mathbf{C}}^e \cdot \bar{\mathbf{T}}^*) : d\bar{\mathbf{C}}^e] - J \sigma_{eq}^2 dJ \tag{C2}$$

Substituting $d\bar{\mathbf{T}}^* = d\bar{\mathbf{T}} - \frac{1}{3}d(\bar{\mathbf{T}} : \bar{\mathbf{C}}^e) \bar{\mathbf{C}}^e - \frac{1}{3}(\bar{\mathbf{T}} : \bar{\mathbf{C}}^e) d\bar{\mathbf{C}}^e$ into Eq. (C2) and noting that $d\bar{\mathbf{C}}^e = -\bar{\mathbf{C}}^e \cdot d\bar{\mathbf{C}}^e \cdot \bar{\mathbf{C}}^e$ and $\bar{\mathbf{T}}^* : \bar{\mathbf{C}}^e = 0$, one obtains,

$$d\sigma_{eq} = \frac{3}{2J^2 \sigma_{eq}} (\bar{\mathbf{C}}^e \cdot \bar{\mathbf{T}}^* \cdot \bar{\mathbf{C}}^e) : d\bar{\mathbf{T}} + \frac{1}{2J^2 \sigma_{eq}} [(\bar{\mathbf{T}} : \bar{\mathbf{C}}^e) \bar{\mathbf{T}}^* + 3\bar{\mathbf{T}}^* \cdot \bar{\mathbf{C}}^e \cdot \bar{\mathbf{T}}^*] : d\bar{\mathbf{C}}^e - \frac{\sigma_{eq}}{J} dJ \tag{C3}$$

From Eq. (7), Eq. (15) and Eq. (C3), the rate of plastic deformation is obtained as

$$\bar{\mathbf{D}}^p = \dot{\bar{\mathbf{E}}}^p = \dot{\bar{\epsilon}}^p \frac{\partial \sigma_{eq}}{\partial \bar{\mathbf{T}}} = \dot{\bar{\epsilon}}^p \frac{3}{2J^2 \sigma_{eq}} \bar{\mathbf{C}}^e \cdot \bar{\mathbf{T}}^* \cdot \bar{\mathbf{C}}^e \tag{C4}$$

Pushing forward into the deformed configuration yields

$$\mathbf{d}^p = \left(\begin{smallmatrix} -\mathbf{T} & -\mathbf{T} \\ \mathbf{F}^e & \mathbf{F}^e \end{smallmatrix} \right)^* \bar{\mathbf{D}}^p = \dot{\bar{\epsilon}}^p \mathbf{n}, \tag{C5}$$

where $\mathbf{n} = \frac{3\sigma'}{2\sigma_{eq}}$ is the normalized flow direction, $\dot{\bar{\epsilon}}^p = \dot{\bar{\epsilon}}^p / J$ is the equivalent plastic strain rate and $\dot{\bar{\epsilon}}^p = \left(\frac{2}{3} \mathbf{d}^p : \mathbf{d}^p \right)^{1/2}$. $\dot{\bar{\epsilon}}^p$ can be determined from the consistency condition. For the perfect plastic model, Eq. (A1) is expressed as

$$\sigma_y \dot{\sigma}_y = \frac{3}{2} \sigma' : \dot{\sigma}' = \frac{3}{2} \sigma' : \dot{\sigma} = 0 \tag{C6}$$

Utilizing Eq. (B4) and noting that $\sigma' : (\mathbf{w}^e \cdot \sigma - \sigma \cdot \mathbf{w}^e) = 0$ in Eq. (C6), leads to

$$\sigma' : \left(\frac{1}{J} \mathbf{D}^e + \mathbf{G}^\sigma - \sigma \mathbf{1} \right) : \mathbf{d}^e = 0 \tag{C7}$$

Since $\mathbf{d}^e = \mathbf{d} - \mathbf{d}^p$, substituting Eq. (C5) into Eq. (C7) yields

$$\dot{\bar{\epsilon}}^p = \frac{\mathbf{n} : \left(\frac{1}{J^e} \mathbf{D}^e + \mathbf{G}^\sigma - \sigma \mathbf{1} \right) : \mathbf{d}}{\mathbf{n} : \left(\frac{1}{J^e} \mathbf{D}^e + \mathbf{G}^\sigma - \sigma \mathbf{1} \right) : \mathbf{n}} \tag{C8}$$

Substituting Eq. (C8) and Eq. (C5) back into Eq. (B5) with $\mathbf{d}^e = \mathbf{d} - \mathbf{d}^p$, the final constitutive law is expressed as

$$\overset{\nabla}{\sigma}^{(e)} = \mathbf{D}^{ep} : \mathbf{d}, \tag{C9}$$

where

$$\mathbf{D}^{ep} = \left(\frac{1}{J} \mathbf{D}^e + \mathbf{G}^\sigma - \sigma \mathbf{1} \right) \frac{\left[\left(\frac{1}{J} \mathbf{D}^e + \mathbf{G}^\sigma - \sigma \mathbf{1} \right) : \mathbf{n} \right] \left[\mathbf{n} : \left(\frac{1}{J} \mathbf{D}^e + \mathbf{G}^\sigma - \sigma \mathbf{1} \right) \right]}{\mathbf{n} : \left(\frac{1}{J} \mathbf{D}^e + \mathbf{G}^\sigma - \sigma \mathbf{1} \right) : \mathbf{n}} \tag{C10}$$

With the assumption of $\mathbf{w}^p = 0$ [41,52], Eq. (C9) can be further simplified as

$$\overset{\nabla}{\sigma} = \mathbf{D}^{ep} : \mathbf{d}, \tag{C11}$$

where $\overset{\nabla}{\sigma} = \dot{\sigma} - \mathbf{w} \cdot \sigma + \sigma \cdot \mathbf{w}$ is the Jaumann derivative of σ .

References

1. Yang Y, Liu D, Xie Y, Lee LJ, Tomasko DL (2007) Low-temperature fusion of polymeric nanostructures using carbon dioxide. *Adv Mater* 19:251–254
2. Ellison CJ, Torkelson JM (2003) The distribution of glass-transition temperatures in nanoscopically confined glass formers. *Nat Mater* 2:695–700
3. Fakhraai Z, Forrest JA (2008) Measuring the surface dynamics of glassy polymers. *Science* 319:600–604
4. Forrest JA (2002) A decade of dynamics in thin films of polystyrene: where are we now. *Eur Phys J E* 8:261–266
5. Sharp JS, Teichroeb JH, Forrest JA (2004) The properties of free polymer surfaces and their influence on the glass transition temperature of thin polystyrene films. *Eur Phys J E* 15:473–487
6. Kim JH, Jang J, Zin WC (2001) Thickness dependence of the glass transition temperature in thin polymer films. *Langmuir* 17:2703–2710
7. Priestley RD, Ellison CJ, Broadbelt LJ (2005) Structural relaxation of polymer glasses at surfaces, interfaces, and in between. *Science* 309:456–459
8. Sharp JS, Forrest JA (2003) Free surfaces cause reductions in the glass transition temperature of thin polystyrene films. *Phys Rev Lett* 91:235701
9. Miyake K, Satomi N, Sasaki S (2006) Elastic modulus of polystyrene film from near surface to bulk measured by nanoindentation using atomic force microscopy. *Appl Phys Lett* 89:31925
10. Torres JM, Stafford CM, Vogt BD (2009) Elastic modulus of amorphous polymer thin films: relationship to the glass transition temperature. *ACS Nano* 3:2677–2685
11. Bohme TR, de Pablo JJ (2002) Evidence for size-dependent mechanical properties from simulations of nanoscopic polymeric structures. *J Chem Phys* 116:9939–9951

12. Yoshimoto K, Jain TS, Nealey PF, De PJ (2005) Local dynamic mechanical properties in model free-standing polymer thin films. *J Chem Phys* 122:144712
13. Tweedie CA, Constantinides G, Lehman KE, Brill DL, Blackman GS, Van Vliet KJ (2007) Enhanced stiffness of amorphous polymer surfaces under confinement of localized contact loads. *Adv Mater* 19:2540–2546
14. Vanlandingham MR, Villarrubia JS, Guthrie WF, Meyers GF (2001) Nanoindentation of polymers: an overview. *Macromol Symp* 167:15–44
15. Zhou J, Komvopoulos K (2006) Surface and interface viscoelastic behaviors of thin polymer films investigated by nanoindentation. *J Appl Phys* 100:114329
16. Saha R, Nix WD (2002) Effects of the substrate on the determination of thin film mechanical properties by nanoindentation. *Acta Mater* 50:23–38
17. Erichsen J, Kanzow J, Schurmann U, Dolgner K, Gunther-Schade K, Strunskus T, Zaporozhchenko V, Faupel F (2004) Investigation of the surface glass transition temperature by embedding of noble metal nanoclusters into mono-dispersed polystyrenes. *Macromolecules* 37:1831–1838
18. Teichroeb JH, Forrest JA (2003) Direct imaging of nanoparticle embedding to probe viscoelasticity of polymer surfaces. *Phys Rev Lett* 91:16101–16104
19. Yang J, Liu C, Yang Y, Zhu B, Lee LJ, Chen H, Jean YC (2009) Analysis of polystyrene surface properties on thin film bonding under carbon dioxide pressure using nanoparticle embedding technique. *J Polym Sci B* 47:1535–1542
20. Hutcheson SA, McKenna GB (2007) Comment on ‘The properties of free polymer surfaces and their influence on the glass transition temperature of thin polystyrene films’ by J.S. Sharp, J.H. Teichroeb and J.A. Forrest. *Eur Phys J E* 22:281–286
21. Sharp JS, Forrest JA, Fakhraai Z, Khomenko M, Teichroeb JH, Dalnoki-Veress K (2007) Reply to comment on ‘The properties of free polymer surfaces and their effect upon the glass transition temperature of thin polystyrene films’ by S.A. Hutcheson and G.B. McKenna. *Eur Phys J E* 22:287–291
22. Stafford CM, Vogt BD, Harrison C, Julthongpipit D, Huang R (2006) Elastic moduli of ultrathin amorphous polymer films. *Macromolecules* 39:5095–5099
23. Rauchs G, Bardon J, Georges D (2010) Identification of the material parameters of a viscous hyperelastic constitutive law from spherical indentation tests of rubber and validation by tensile tests. *Mech Mater* 42:961–973
24. Chen Y (2009) Reformulation of microscopic balance equations for multiscale materials modeling. *J Chem Phys* 130:134706
25. Lyulin AV, Balabaev NK, Mazo MA, Michels MA (2004) Molecular dynamics simulation of uniaxial deformation of glassy amorphous atactic polystyrene. *Macromolecules* 37:8785–8793
26. Lyulin AV, Michels MA (2007) Time scales and mechanisms of relaxation in the energy landscape of polymer glass under deformation: direct atomistic modeling. *Phys Rev Lett* 99:85504
27. Vorselaars B, Lyulin AV, Michels MAJ (2009) Deforming glassy polystyrene: influence of pressure, thermal history, and deformation mode on yielding and hardening. *J Chem Phys* 130:74905
28. Simoes R, Cunha AM, Brostow W (2006) Molecular dynamics simulations of polymer viscoelasticity: effect of the loading conditions and creep behaviour. *Model Simul Mater Sci Eng* 14:157
29. van Workum K, de Pablo JJ (2003) Computer simulation of the mechanical properties of amorphous polymer nanostructures. *Nano Lett* 3:1405–1410
30. Alleman C, Srivastava A, Ghosh S (2011) Molecular dynamics simulations of carbon dioxide assisted bonding of polystyrene thin films. *J Polym Sci B* 49:1183–1194
31. Srivastava A, Alleman C, Ghosh S, Lee LJ (2010) Molecular dynamics simulation based evaluation of glass transition temperatures of polystyrene in the presence of carbon dioxide. *Model Simul Mater Sci Eng* 18:65003
32. Srivastava A, Ghosh S (2010) Evaluating the glass transition temperature of polystyrene by an experimentally validated molecular dynamics model. *Int J Multiscale Comput Eng* 8:535–547
33. Smith SW, Hall CK, Freeman BD (1997) Molecular dynamics for polymeric fluids using discontinuous potentials. *J Comput Phys* 134:16–30
34. Harmandaris VA, Adhikari NP, van der Vegt VFA, Kremer K (2006) Hierarchical modeling of polystyrene: from atomistic to coarse-grained simulations. *Macromolecules* 39:6708–6719
35. Wick CD, Martin MG, Siepmann JI (2000) Transferable potentials for phase equilibria. 4. united-atom description of linear and branched alkenes and alkyl benzenes. *J Phys Chem B* 104:8008–8016
36. Han J, Boyd RH (1996) Molecular packing and small-penetrant diffusion in polystyrene: a molecular dynamics simulation study. *Polymer* 37:1797–1804
37. Subramanian AK, Sun CT (2008) Continuum interpretation of virial stress in molecular simulations. *Int J Solids Struct* 45:4340–4346
38. Zimmerman JA, Webb EB, Hoyt JJ, Jones RE, Klein PA (2004) Calculation of stress in atomistic simulation. *Model Simul Mater Sci Eng* 12:S319–S332
39. Zhou M (2003) A new look at the atomic level virial stress: on continuum-molecular system equivalence. *Proc R Soc A* 459:2347–2392
40. Mark JE (1999) *Polymer data handbook*. Oxford University Press, New York
41. Moran B, Ortiz M, Shih CF (1990) Formulation of implicit finite-element methods for multiplicative finite deformation plasticity. *Int J Numer Methods Eng* 29:483–514
42. Bedalov T (2007) Modeling hyperelastic behavior of rubber: a novel invariant-based and a review of constitutive models. *J Polym Sci B* 45:1713–1732
43. Hartmann S (2001) Parameter estimation of hyperelasticity relations of generalized polynomial-type with constraint conditions. *Int J Solids Struct* 38:7999–8018
44. Arruda EM, Boyce MC (1993) A three-dimensional constitutive model for the large stretch behavior of rubber elastic materials. *J Mech Phys Solids* 41:389–412
45. Ogden RW (1972) Large deformation isotropic elasticity—on the correlation of theory and experiment for incompressible rubberlike solids. *Proc R Soc A* 326:565–584
46. Gendy AS, Saleeb AF (2000) Nonlinear material parameter estimation for characterizing hyper elastic large strain models. *Comput Mech* 25:66–77
47. Saleeb AF, Chang TYP, Arnold SM (1992) On the development of explicit robust schemes for implementation of a class of hyperelastic models in large-strain analysis of rubbers. *Int J Numer Methods Eng* 33:1237–1249
48. Gilmour IW, Trainor A, Haward RN (1979) Elastic moduli of glassy polymers at low strains. *J Appl Polym Sci* 23:3129–3138
49. Bower AF (2009) *Applied mechanics of solids*. CRC Press, Boca Raton
50. Loggi LT (1998) An experimental characterization of the tensile behavior of polystyrene. Dissertation, Rochester Institute of Technology
51. Baljon AR, Williams S, Balabaev NK, Paans F, Hudzinskyy D, Lyulin AV (2010) Simulated glass transition in free-standing thin polystyrene films. *J Polym Sci B* 48:1160–1167
52. Agah-Tehrani A, Lee EH, Mallett RL, Onat ET (1987) The theory of elastic-plastic deformation at finite strain with induced anisotropy modeled as combined isotropic-kinematic hardening. *J Mech Phys Solids* 35:519–539